PCCP

ROYAL SOCIETY OF CHEMISTRY

PAPER

View Article Online
View Journal | View Issue

Cite this: *Phys. Chem. Chem. Phys.*, 2023, **25**, 1081

Enhanced stability of sub-nanometric iridium decorated graphitic carbon nitride for H_2 production upon hydrous hydrazine decomposition†

Silvio Bellomi, [a] Ilaria Barlocco,[a] Xiaowei Chen, [b] Juan J. Delgado,[b] Rosa Arrigo, [c] Nikolaos Dimitratos, [de] Alberto Roldan [*f] and Alberto Villa [*a]

Received 20th September 2022,
Accepted 29th November 2022

DOI: 10.1039/d2cp04387d

rsc.li/pccp

Stabilizing metal nanoparticles is vital for large scale implementations of supported metal catalysts, particularly for a sustainable transition to clean energy, *e.g.*, H_2 production. In this work, iridium sub-nanometric particles were deposited on commercial graphite and on graphitic carbon nitride by a wet impregnation method to investigate the metal–support interaction during the hydrous hydrazine decomposition reaction. To establish a structure–activity relationship, samples were characterized by transmission electron microscopy and X-ray photoelectron spectroscopy. The catalytic performance of the synthesized materials was evaluated under mild reaction conditions, *i.e.* 323 K and ambient pressure. The results showed that graphitic carbon nitride (GCN) enhances the stability of Ir nanoparticles compared to graphite, while maintaining remarkable activity and selectivity. Simulation techniques including Genetic Algorithm geometry screening and electronic structure analyses were employed to provide a valuable atomic level understanding of the metal–support interactions. N anchoring sites of GCN were found to minimise the thermodynamic driving force of coalescence, thus improving the catalyst stability, as well as to lead charge redistributions in the cluster improving the resistance to poisoning by decomposition intermediates.

Introduction

Metal nanoparticles (NPs) dispersed on carbonaceous supports are of high interest in catalysis. In particular, platinum-group-metals, *i.e.* Ru, Rh, Pd, Os, Ir and Pt, remain essential for many sustainable chemical processes, including biomass valorisation and hydrogen production, due to their excellent catalytic performances and durability.[1,2]

Establishing a structure–activity and stability relationship in heterogeneous catalysis is challenging.[3] The dependency of the catalytic activity upon particle size, structure of the active phase and support effects has been demonstrated for several catalytic processes[4] thanks to recent advances in characterization techniques.[5,6] Indeed, the number and composition of accessible conformations at operative conditions are strongly dependent upon the NP diameter, leading to dimension-specific catalytic activities where "every atom counts". Usually, the smaller the particle size, the higher is the catalyst performance due to an enhanced number of superficial atoms able to react with the substrates.[7,8]

Among the many reports available in the literature regarding supported metal particles as catalysts,[4,9] remarkable results were obtained using NPs with sizes below 2 nm. For example, the activity of Rh NPs in the hydrogenation of cyclohexene[10] and phenols[11] is greatly enhanced when particle sizes are 0.4 nm and 1.3 nm, respectively. However, Rogers and co-workers[12] found that Pd nanoclusters of about 20 atoms have lower durability than larger NPs for the furfural hydrogenation reaction. Indeed, despite the intriguing properties related to sub-nanometric metal clusters, one of the biggest challenges is still finding practical ways to stabilise them against migration and ripening phenomena.

The support plays a fundamental role in stabilizing metal clusters, avoiding undesired sintering processes.[13,14] Carbon materials are highly attractive as catalyst supports, because of their

[a] *Dipartimento di Chimica, Università degli Studi di Milano, via Golgi 19, I-20133 Milano, Italy. E-mail: alberto.villa@unimi.it*
[b] *Departamento de Ciencia de los Materiales, Ingeniería Metalúrgica y Química Inorgánica, Facultad de Ciencias, Universidad de Cádiz, Campus Río San Pedro, Puerto Real (Cádiz) E-11510, Spain*
[c] *School of Science, Engineering and Environment, University of Salford, M5 4WT, Manchester, UK*
[d] *Dipartimento di Chimica Industriale "Toso Montanari", Alma Mater Studiorum Università di Bologna, Viale Risorgimento 4, Bologna 40126, Italy*
[e] *Center for Chemical Catalysis-C3, Alma Mater Studiorum Università di Bologna, Viale Risorgimento 4, Bologna 40136, Italy*
[f] *Cardiff Catalysis Institute, School of Chemistry, Cardiff University, Main Building, Park Place, CF10 3AT, Cardiff, UK. E-mail: RoldanMartinezA@cardiff.ac.uk*
† Electronic supplementary information (ESI) available. See DOI: https://doi.org/10.1039/d2cp04387d

relatively low costs and high tunability of the physicochemical properties. Indeed, chemical modification of a carbon surface can improve the stabilization of few-atom clusters and single atoms,[15–20] and strongly influence the nature of the metal species, in a way which resembles organic ligands in organometallic catalysis, thus opening up the opportunity to realize high site specificity.[20–23] The presence of heteroatoms (*e.g.* N, O, B, and P) and surface defects provide three main advantages: (i) to act as nucleation/growth sites for metal clusters,[24,25] (ii) to stabilize metal clusters through coordinative bonds suppressing undesired sintering processes,[21,22] and (iii) to alter the cluster electronic configuration to facilitate adsorption/desorption of substrates, thus enhancing reaction rates. In a recent study Liu and co-workers, it was demonstrated that Ir nanodots embedded in a carbon skeleton with an average size of 1.19 nm were remarkably stable in the electrocatalytic nitrogen reduction reaction (NRR), exhibiting excellent electrocatalytic NRR performances under both acidic and alkaline conditions.[26] Concerning heteroatom stabilization, Kim and co-workers observed that sub-2 nm Pt NPs deposited on O-doped carbon enhanced the catalytic activity in the oxygen reduction reaction (ORR) with respect to the pristine support.[27] In formic acid decomposition (FAD), the effect of dopants (*i.e.* O, P and N) was unveiled, highlighting a great improvement in the catalytic performances and stability of Pt NPs.[28] Xu and co-workers reported an exceptionally high catalytic activity for FAD (14 400 h^{-1}) performed over Pd NPs immobilized in N-doped hierarchically porous carbons at 333 K. In addition, the N functionalities enabled them to stabilize ultra-fine nanoparticles (1.1 ± 0.2 nm), enhancing the catalyst activity with respect to the pristine counterparts.[29] Different electrocatalysis reports also confirmed the possibility of stabilizing nanoparticles below 2 nm by employing N-functionalised carbon materials.[30–35] Recent studies indicated graphitic carbon nitride as an ideal support for stabilizing small NPs,[36,37] nanoclusters,[38,39] and single atom species[39–45] due to its unique properties.[46] The peculiar electronic structure and the N-rich framework composed of amine-bridged tri/heptazine moieties in these systems provide many adsorption sites for grafting metal clusters on their surface.[47]

Hydrazine (N_2H_4) is one of most promising hydrogen carriers.[48,49] It is a carbon-free fuel, and has a hydrogen content of 12.5 wt%.[50] However, hydrazine possesses an intrinsic hypergolic nature, namely, the risk of explosion is one of the most serious problems related to its handling, especially in the presence of active metals that may catalyze its decomposition.[51] One solution to this challenge is N_2H_4 dilution in water, forming hydrous hydrazine ($N_2H_4 \cdots H_2O$), which contains an 8 wt% intrinsic stoichiometric content of hydrogen.[52,53] $N_2H_4 \cdots H_2O$ is reported to decompose catalytically through two different pathways:[54]

$$N_2N_4 \rightarrow N_2(g) + 2H_2(g) \quad \Delta H^0 = -95.4 \text{ kJ mol}^{-1} \qquad (1)$$

$$3N_2N_4 \rightarrow N_2(g) + 4NH_3(g) \quad \Delta H^0 = -157.0 \text{ kJ mol}^{-1} \qquad (2)$$

The first reaction (eqn (1)) represents the complete reforming pathway, where molecular hydrogen and nitrogen are produced. The second path (eqn (2)) produces nitrogen and ammonia and is the thermodynamically favored process. The selectivity of the process depends upon several reaction conditions, such as pressure, temperature and nature of the catalyst.[55–57] Previous studies have shown that iridium is effective in the catalytic decomposition of hydrous hydrazine. Singh and co-workers reported the activity of a series of monometallic nanoparticles (Rh, Co, Ir, Cu, Ni, Fe, Pt and Pd) for the hydrous hydrazine decomposition and, at 298 K, although very active, Ir was only able to achieve 7% of H_2 selectivity, and no information on the stability of the catalysts was reported.[58] The low Ir selectivity was confirmed by computational Density Functional Theory (DFT) studies of hydrazine decomposition over an Ir(111) slab, underlining the ability of the surface to decompose the substrate preferentially through the incomplete decomposition pathways (eqn (2)).[59] Jang and co-workers prepared honeycomb Ir NPs immobilized on γ-Al_2O_3 through a soak-dry procedure, with a nominal metal loading of 2 wt% (2 wt% Ir/γ-Al_2O_3). The authors demonstrated the ability of such catalysts to decompose hydrous hydrazine at ambient temperature, but no detailed information on catalytic activity, stability and H_2 selectivity was reported.[60] Furthermore, Motta and co-workers synthesized by a decomposition–precipitation method sub-nanometric (>2 nm) Ir NPs supported on CeO_2 (1 wt% Ir/CeO_2) and tested it in the hydrous hydrazine decomposition, varying the reaction temperature. They demonstrated that increasing the reaction temperature resulted in a higher activity but a lower selectivity toward H_2.[57]

In this work, Ir sub-nanometric clusters supported on graphitic carbon materials (graphite and GCN) were studied in the hydrous hydrazine decomposition reaction. Graphite and GCN present comparable electronic and morphological properties, but a remarkably different N intrinsic content, which allowed us to rationalise the enhanced stability of supported sub-nanometric Ir particles on carbonaceous supports and unveil the effect of N-functionalities. To disclose structure–activity correlations and metal–support interactions, fresh and used catalysts were characterized by HR-TEM and XPS in combination with computational techniques. The combined experimental and computational approach presented herein provided an in depth understanding of the enhanced stability observed over GCN at the atomistic scale and of the role of metal–support interactions.

Experimental method

Materials and chemicals

Graphite was obtained from Johnson Matthey. $IrCl_3$ xH_2O (99.9%), $N_2H_4 \cdots H_2O$ (98%), sodium hydroxide (NaOH, $\geq$98%), molten cyanamide, Ludox HS40 SiO_2 particles, NH_4HF_2, $NaBH_4$ and ethanol were acquired from Sigma-Aldrich.

Catalyst synthesis

GCN synthesis. The carbon nitride sample was prepared following the procedure reported in the literature.[61] Accordingly, molten cyanamide (1 g, 24 mmol; Sigma-Aldrich) was heated and stirred at 343 K, and 1 g of a 40 wt% dispersion of SiO_2 particles (Ludox HS40, Aldrich) in water was added dropwise to establish a

40 vol% porosity. The resulting transparent mixture was then heated at a rate of 4.5 K min^{-1} over 2 h to reach a temperature of 848 K and then kept at this temperature for another 4 h. The resulting yellow powder was treated with 25 mL of 4 M NH_4HF_2 under continuous stirring at room temperature for 2 days to remove the silica template in a closed polypropylene bottle flushed with nitrogen. The powder was then centrifuged and washed three times with distilled water and twice with ethanol. Finally, the powder was dried at 343 K under vacuum for several hours.

Iridium wet impregnation procedure

In a typical wet impregnation procedure, slightly varied from the work of Shao and co-workers,[36] a final MeOH volume of 100 mL was employed. In a 250 mL round bottom flask, 0.5 g of the desired support was introduced and left under stirring (1250 rpm) for 15 min. After the specified time, the temperature was slowly increased up to 323 K, the desired amount of precursor ($IrCl_3$ xH_2O, 99.9%) was introduced, and the mixture was slowly heated up to 343 K and left under reflux conditions for 8 h. The amount of support and precursor were calculated to have a nominal metal loading of 1 wt%. After the specified time, a 20-fold molar excess of aqueous $NaBH_4$ was quickly added, and the reaction mixture was left under stirring for 1 h to ensure complete reduction of the impregnated precursor. The solid was filtered, washed several times with EtOH (1 L g^{-1}) and water (1 L g^{-1}), and dried overnight at RT in air.

Catalytic tests

Liquid phase $N_2H_4\cdot\cdot H_2O$ decomposition was performed at a constant reaction temperature of 323 K, under kinetic conditions,[57] using a 35 mL two-necked round bottom flask, with one of the flask's necks connected to the pressure detection sensor. Gaseous products evolution was monitored through the *Man On the Moon X102* kit measuring the partial pressures of the released product, as reported in several reports concerning H_2 production.[62–64] In a typical procedure, the required amount of catalyst ($N_2H_4\cdot\cdot H_2O$/metal molar ratio 1000/1) was added to the reactor, where 5.0 mL of a 0.5 M NaOH aqueous solution was placed and heated at the desired temperature, until the registered pressure exhibited a plateau, indicating that equilibrium has been achieved. Once equilibrated, the pressure was released to avoid over-pressures within the reactor. Finally, 300 μL of a 3.3 M hydrous hydrazine aqueous solution was injected into the reactor through a vacuum septum, using a syringe, with the final mixture stirring at 1400 rpm. Once the substrate was injected, the data collection started with a sampling time of 0.3 s until the end of the decomposition reaction, indicated by a pressure plateau. To ensure experimental reproducibility and assess measuring uncertainty, all the catalytic tests were performed three times. Selectivity towards H_2 generation (x) was evaluated based on eqn (3):

$$3N_2H_4 \rightarrow 4(1-x)NH_3 + 6xH_2 + (1+2x)N_2 \qquad (3)$$

The released gaseous products were allowed to pass into a trap containing a 0.05 M HCl aqueous solution to ensure the removal of NH_3,[65] if any, hence the gas pressure measured during the reaction contained only N_2 and H_2, enabling us to obtain the molar ratio (λ) as $\frac{n(H_2+N_2)}{n(N_2H_4)}$ by means of the perfect gas law ($pV = nRT$). Therefore, H_2 selectivity was calculated through eqn (4):

$$x = \frac{3\lambda - 1}{8}, \quad \left[\lambda = \frac{n(H_2+N_2)}{n(N_2H_4)}\left(\frac{1}{3} \leq \lambda \leq 3\right)\right] \qquad (4)$$

Catalytic activity was calculated as the ratio between moles of converted substrate and metal moles, normalized with respect to the reaction time (t). All the metal species were considered active in the hydrous hydrazine decomposition. Considering the high number of sampling data, it was possible to calculate the initial activity for time approaching zero ($t \rightarrow 0$) through numerical data treatment. Data analysis and elaboration were performed with in-house developed Python scripts based on Numpy[66] and Scipy,[67] well-established libraries for numerical analysis.

Catalysts characterization

TEM experiments were performed on a double Cs aberration-corrected FEI Titan3 Themis 60–300 microscope equipped with a monochromator, a X-FEG gun and a high efficiency XEDS ChemiSTEM, which consists of 4-windowless SDD detectors. HR-STEM imaging was performed at 200 kV and using a high-angle annular dark-field (HAADF) detector with a camera length of 11.5 cm. The HAADF-STEM technique is sensitive to the atomic number of the elements, whose intensity is roughly proportional to the square of the atomic number (Z^2) and makes it possible to distinguish small nanoparticles supported on light supports. XEDS mappings were performed using a beam current of 200 pA and a dwell time per pixel of 128 μs. To improve the visual quality of the elemental maps obtained, these were filtered using a Gaussian blur of 0.8 using Velox software. Based on the STEM-HAADF images of the catalysts, the diameters of more than 200 metal particles randomly selected were measured and the corresponding metal particle size distributions (PSD) were determined. Based on these PSDs, mean particle diameter (d) was calculated according to the following expression: $d = n_i d_i / n_i$, where $n_i \geq 200$. For average particle size calculation ImageJ software was used.

X-ray photoelectron spectroscopy (XPS) analyses were performed on a Kratos Axis Ultra DLD instrument. Spectra were recorded using monochromatized Al Kα radiation (1486.6 eV), with an X-ray power of 150 W. The spectrometer was operated in the Constant Analyser Energy mode, with a pass energy of 20 eV. Powder samples were pressed into pellets, which were stuck on double-sided adhesive conducting polymer tape. Surface charging effects were compensated by making use of the Kratos coaxial neutralization system. XPS data analysis was performed with CasaXPS Software, version 2319PR1-0, developed by Neal Fairley (Casa Software Ltd, 2013). The N1s XPS peaks were fitted using the model reported in ref. 68 for the GCN and ref. 69 the graphite systems. The C1s XPS peaks were fitted using the model reported in ref. 68 for the GCN

and ref. 70 for the graphite systems. The Ir 4f was fitted using the model reported in ref. 71. The O1s XPS peaks were fitted according to the model reported in ref. 70. Table S1 (ESI†) summarizes the fitting models employed.

Inductively coupled plasma optical emission spectroscopy (ICP-OES) analyses, using a PerkinElmer Optima 8000 emission spectrometer, were performed to confirm the Ir metal loading and to detect metal leaching in the reaction solution.

Computational details

Periodic plane-wave density functional theory (pw-DFT) calculations were carried out using the Vienna *Ab-initio* Simulation Package (VASP).[72,73] In order to take into account the correlation–exchange electronic contributions, the Perdew–Burke–Ernzerhof (PBE) functional was employed, based on previous reports on metal–support interaction,[31,74] with a kinetic energy of 520 eV chosen as the cutoff value for the expansion of the plane-waves basis set. All calculations employed long-range dispersion correction as proposed by the Grimme – DFT-D3 method,[75,76] which shows an improvement on pure DFT to evaluate molecular interactions.[77–80] The optimization thresholds for electronic energies and ionic forces relaxation were respectively 10^{-6} eV and 0.02 eV Å^{-1}. Accurate electronic structures were obtained by means of the tetrahedron method as implemented in VASP. The Brillouin zone was sampled using a 5 × 5 × 1 Γ-centred k-point mesh generated through the Monkhorst–Pack method, minimising any Pulay stress.[81] We calculated the Bader charges difference (BCD) and charge density difference (CDD) using eqn (5) and (6) respectively.

$$q(\text{BCD}) = q(\text{Combined}) - q(\text{Surf}) - q(\text{Ir}_{15}) \quad (5)$$

$$\rho(\text{CCD}) = \rho(\text{Combined}) - \rho(\text{Surf}) - \rho(\text{Ir}_{15}) \quad (6)$$

where $q(i)$ and $\rho(i)$ respectively indicates the charge and electron density of species i. Adsorption (E_{ads}) and adhesion (E_{adh}) energies were calculated using eqn (7) and (8). Where E_{Cluster} is the cluster energy, and E_{Surf} and E_{Surf}* refer to the energy of the relaxed pristine surface as isolated and the naked surface with the geometry of the adsorbed system, respectively, and, hence, including and excluding the deformation energy contributions. The surface deformation (E_{def}) energy was quantified using eqn (9). Data visualization was performed by means of different tools, including VESTA[82] and in-house developed python scripts (Matplotlib[83] and Mayavi[84]).

$$E_{\text{ads}} = E_{\text{System}} - E_{\text{Surf}} - E_{\text{Cluster}} \quad (7)$$

$$E_{\text{ads}} = E_{\text{System}} - E_{\text{Surf}}^{*} - E_{\text{Cluster}} \quad (8)$$

$$E_{\text{def}} = E_{\text{ads}} - E_{\text{adh}} \quad (9)$$

Simulation models

To evaluate the key features of the catalysts, different simulation models were employed. Represented in Fig. S1 (ESI†), we modelled pristine (PG) and single vacancy (SV) graphene representing graphite, and graphitic N (gN) and triple pyridinic N (3pN) to model GCN. All surfaces were generated with the Atomic Simulation Environment (ASE)[85] and modelled on a $p(8 \times 8)$ graphene slab supercell with 27 Å vacuum along the c-axis to avoid any interaction between adjacent images.

A metal–cluster model simulating the true size of the supported nanoparticles experimentally observed is prohibitively expensive to compute using electronic structure methods. For this reason, a simplified model cluster containing 15 Ir atoms was modelled on the graphitic support. Indeed, cluster–support interfaces have been shown to participate in many reactions[74,86–90] and, therefore, it is essential to consider them on realistic catalytic models.

The most stable conformations of the Ir_{15} clusters on the different surfaces, *i.e.*, PG, SV, gN and 3pN, were found from ~800 cluster structures generated by an in-house modified version of the unbiased Birmingham Parallel Genetic Algorithm (BPGA),[91] and evaluated at the DFT level following a three-step process. The first step in the global optimisation protocol is the generation of ~200 supported clusters for each surface, considering a pool size of 10 members with crossover and mutation operation procedures performed by means of randomization and displacement operators, respectively. The initial pool members were randomly generated with a cluster to surface height of 2.0 Å. A mutation rate of 10% was employed to guarantee the generational variety among the structures.[90] It is worth noting that, for each surface, the same number of generated structures was considered, unbiases leading to a final pool of 10 fittest NP structures, *i.e.*, the most stable. The energy of all these structures was determined by VASP using a soft optimization protocol, *i.e.*, thresholds for electronic and ionic relaxation energies respectively of 10^{-4} eV and 10^{-3} eV, Γ-point only and a frozen support geometry. An increased number of initial non-self-consistent steps and linear-mixing involving the metal d-orbitals were found to improve the wavefunction convergence. The Brillouin-zone evaluation was eased using the second order Methfessel–Paxton method with a smearing width of 0.1 eV. In the second step, the final pool of 10 elements was re-optimised with an enhanced k-space sampling (5 × 5 × 1, Γ-centred Monkhorst–Pack k-point mesh) and thresholds for electronic energies and ionic forces of 10^{-6} eV and 0.02 eV Å^{-1}, while maintaining the support frozen. Finally, the fittest candidate was fully relaxed, *i.e.*, NP and support, and the electronic structure was investigated with the accurate computational settings explained in the computational details section.

Results and discussion

Commercial graphite and synthesized GCN were employed as supports for Ir nanoparticles (1 wt%) prepared by a wet impregnation (WI) procedure. Firstly, the catalysts were evaluated in the hydrous hydrazine decomposition reaction at 323 K with a $N_2H_4{\cdot}{\cdot}{\cdot}H_2O$: catalyst molar ratio of 1000 : 1. Stability tests up to 5 repeated reaction runs were performed. Then, fresh catalysts and used catalysts were thoroughly characterized using XPS and TEM to elucidate the structure–activity and stability relationships rationalizing the kinetic results. Finally, a detailed computational investigation was combined with the characterization

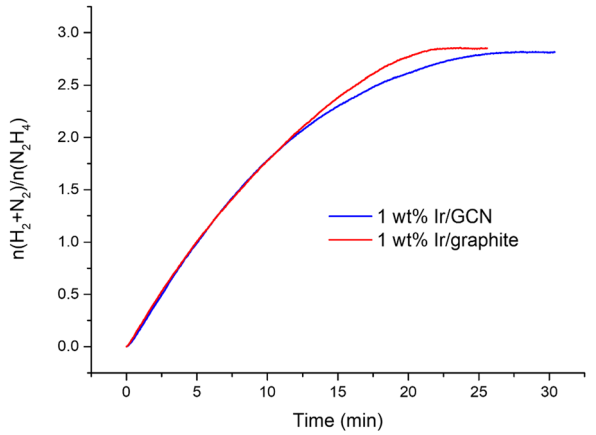

Fig. 1 Kinetic profiles of 1 wt% Ir/graphite (red) and 1 wt% Ir/GCN (blue) catalysts for hydrous hydrazine decomposition. All tests were performed at 323 K and 1400 rpm, using 300 μL of a hydrazine solution 3.3 M in 5 mL of NaOH 0.5 M and a $N_2H_4\cdots H_2O$: catalyst molar ratio of 1000 : 1. A sampling time of 0.3 s was employed to obtain continuous kinetic profiles.

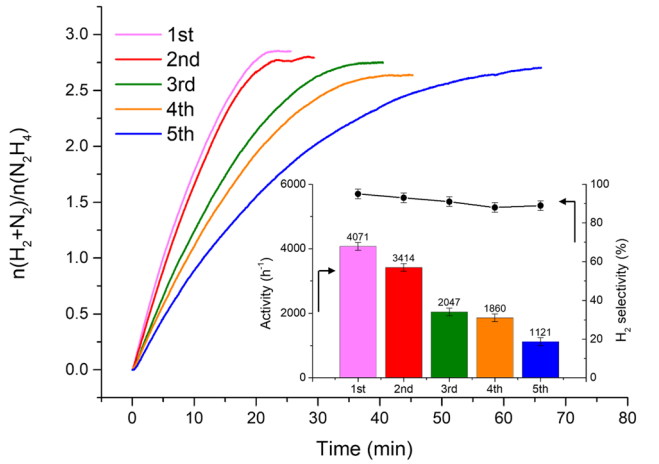

Fig. 2 Stability tests for 1 wt% Ir/graphite. The insets are the catalytic activity (left axis) and H_2 selectivity (right axis) trends along repeated cycles. All tests were performed at 323 K and 1400 rpm, using 300 μL of a 3.3 M hydrazine solution in 5 mL of 0.5 M NaOH and a $N_2H_4\cdots H_2O$: catalyst molar ratio of 1000 : 1. A sampling time of 0.3 s was employed to obtain continuous kinetic profiles.

and kinetic results to obtain unique atomic scale insights on the metal support interactions explaining the different catalytic trends observed in the stability tests.

Catalytic activity

The catalytic performances of Ir NPs deposited on graphite (Ir/graphite) and GCN (Ir/GCN) were evaluated in liquid-phase hydrous hydrazine decomposition. The pressure of evolved gaseous products (H_2 and N_2) was recorded and elaborated, resulting in a $\frac{n(H_2+N_2)}{n(N_2H_4)}$ *versus* time profile, where $n(H_2 + N_2)$ and $n(N_2H_4)$ are respectively the moles of gaseous products and initial substrate. Higher $\frac{n(H_2+N_2)}{n(N_2H_4)}$ ratio, higher activity and higher selectivity toward H_2.

The kinetic profiles for the two catalysts were examined for 30 minutes of reaction (Fig. 1), where a pressure plateau indicates the end of the hydrous hydrazine decomposition reaction, which means that hydrous hydrazine conversion reaches the maximum. The two catalysts resulted in comparable profiles, exhibiting excellent initial activities of 4024 h^{-1} and 3654 h^{-1}, calculated for $t \rightarrow 0$, and remarkable high H_2 selectivity of 95% and 94% respectively for Ir/graphite and Ir/GCN, calculated at the pressure plateau.

A crucial feature of a catalyst for commercial applications is the durability over repeated reaction runs, especially when precious metals such as Ir are involved. For this reason, stability tests were performed on both Ir/graphite and Ir/GCN, by filtering and reusing the catalyst without any further treatment.

Fig. 2 shows that the Ir/graphite rapidly deactivates decreasing up to 70% from its initial activity (from 4071 h^{-1} to 1121 h^{-1}) after five repeated cycles, with a slight decrease of the H_2 selectivity (from 95 to 89%). In contrast, the Ir/GCN exhibited remarkable stability (3675 h^{-1} to 3241 h^{-1}) and almost constant H_2 selectivity (from 94 to 92%) after five cycles of the reaction (Fig. 3). In both cases, the H_2 selectivity is still very high after 5 runs of catalytic tests.

Catalyst characterization

Fresh and used materials were thoroughly characterized to disclose the structure–stability relationship. Information on the catalyst morphology, *e.g.*, distribution on the support, particle size and structural changes after stability tests, were obtained through TEM analysis. XPS was employed to investigate the surface composition, *e.g.*, superficial composition, oxidation state and exposed iridium atoms (fresh and after 5 repeated reaction cycles).

Fig. 4 shows representative STEM-HAADF images of the fresh Ir/graphite catalysts and those used for 5 runs. In the fresh catalyst, small Ir particles in the range from 0.5 to 4.0 nm can be observed, presenting a mean size of 1.9 ± 0.4 nm. The mean size changes only slightly in the sample used for 5 runs, 2.1 ± 0.5 nm (Fig. 4). Ir particles preferentially located at the graphite planes boundaries and agglomerated to form a net were observed (Fig. S2 and S3, ESI†).

On the other hand, the Ir clusters were homogeneously distributed and well-dispersed on GCN (Ir/GCN), in agreement with the N anchoring sites observed from HAADF-STEM (Fig. S4, ESI†). The Ir clusters presented a narrow particle size distribution, from 0 to 3.5 nm with a mean size of 1.8 ± 0.4 nm, which remained constant, 1.7 ± 0.4 nm, after their use in the N_2H_4 decomposition reaction for 5 repeated runs (Fig. 5). Noticeably, in Ir/GCN, many small clusters and single atoms (SAs) were observed either on fresh or 5 runs used catalysts (Fig. 5 and Fig. S5, ESI†). Nonetheless, the particle size distributions of the catalysts were obtained without considering the SAs due to the increased complexity of the related statistic. Overall, the TEM results indicate that both catalysts exhibit exceptionally good structural stability after 5 reaction runs.

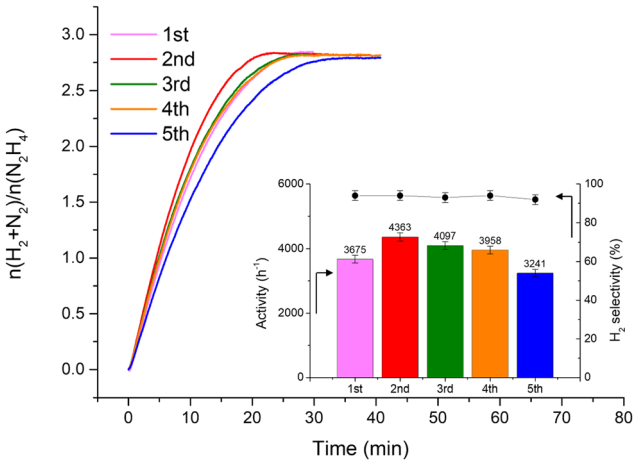

Fig. 3 Stability tests for 1 wt% Ir/GCN. The insets are the catalytic activity (left axis) and H_2 selectivity (right axis) trends along repeated cycles. All tests were performed at 323 K and 1400 rpm, using 300 μL of a 3.3 M hydrazine solution in 5 mL of 0.5 M NaOH and a $N_2H_4\cdot\cdot H_2O$: catalyst molar ratio of 1000 : 1. A sampling time of 0.3 s was employed to obtain continuous kinetic profiles.

Table 1 summarizes the chemical species observed on the surface and their atomic concentration as obtained from the survey analysis of the XPS spectra. The results show that Ir/GCN, either fresh or used, presents a higher extent of exposed metal (1.3 and 1.0% respectively for fresh and 5 runs used) than graphite supported particles (0.8 and 0.3% respectively for fresh and 5 runs used). This indicates a better dispersion of sub-nanometric particles over GCN, as well as an enhanced stability under reaction conditions. Moreover, Ir/graphite, after 5 runs, exhibited an increase of 1.2 At% of N 1s components, suggesting a deactivation due to poisoning of the catalysts from residual hydrous hydrazine decomposition intermediates.

For all the catalysts, high-resolution (HR) C 1s, N 1s, and Ir 4f XPS spectra were fitted (Fig. 6 and Fig. S6–S9, ESI†) using a fitting model as described in the experimental section. For the C 1s region of all the graphite samples, four main peaks were considered: the most intense peak at a binding energy (BE) of 284.3–284.4 eV is assigned to C in sp^2 bonding configuration; the peaks at BEs of 285.1–285.2, 285.6–285.7 and 286.2–286.3 eV are assigned to C in sp^3 configuration, C–O and C═O respectively.[92] C 1s XPS spectra for GCN samples show an asymmetric peak of BE 285.4–285.5 eV, assigned to the C–N═C moieties.[68] A more intense symmetric peak of BE 288.7–288.8 eV, related to C═C components was also observed.[93] It is worth noting that after Ir deposition on graphite, the C 1s spectra (Fig. S6, ESI†) remain largely unchanged, indicating the presence of similar C species with a similar relative distribution. Differently, for GCN a net decrease in the intensity ratio between C–N═C and C═C peaks was observed after the sub-nanometric particles immobilization (Fig. S7, ESI†) indicating a smaller amount of superficial C–N═C moieties. We postulate that this is an electronic effect due to the interaction of the Ir clusters with the C–N═C sites. Furthermore, an additional decrease in the intensity ratio is observed after the first reaction run of stability tests ($\frac{I_{C-N-C}}{I_{C-C}}$ from 1.67 to 1.44, Table 2), indicating that, upon reaction, Ir clusters are mobilised and redeposited as smaller clusters, covering more C–N═C sites. The increase of the catalytic activity of Ir/GCN between the first and the second run (from 3675 to 4363 h^{-1}, Fig. 3) could be a consequence of this structural transformation.

For GCN, the N 1s region (Fig. S8, ESI†) was fitted with four components, consistent with the literature on heptazine-based carbon nitride. Namely, pyridine-like (C═N, 398.5–398.6 eV), conjugated amines (C═N–H, 399.9–400.0 eV), quaternary N (400.9–401.0 eV) and NO_x species (404.1–404.2 eV).[94,95] Upon sub-nanometric particles immobilization, the N 1s spectra exhibited an increase in the intensity ratios between qN and C═N–H peaks with respect to the C═N one, indicating a higher coverage of pyridinic sites, thus highlighting a more favourable interaction. Table 2 summarizes the intensity ratio trend of C–N═C with C═C $\left(\frac{I_{C-N-C}}{I_{C-C}}\right)$, qN with C═N $\left(\frac{I_{qN}}{I_{C=N}}\right)$ and C═N–H with C═N $\left(\frac{I_{C=N-H}}{I_{C=N}}\right)$ for the nitride samples.

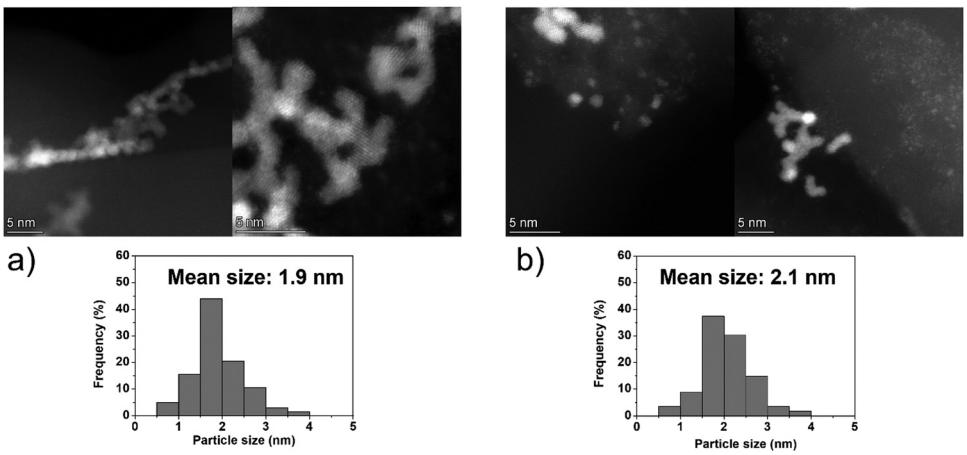

Fig. 4 Representative HAADF-STEM images and Ir particle size distribution of 1 wt% Ir/graphite, (a) fresh and (b) after 5 runs. Inset histograms show the particle size distribution.

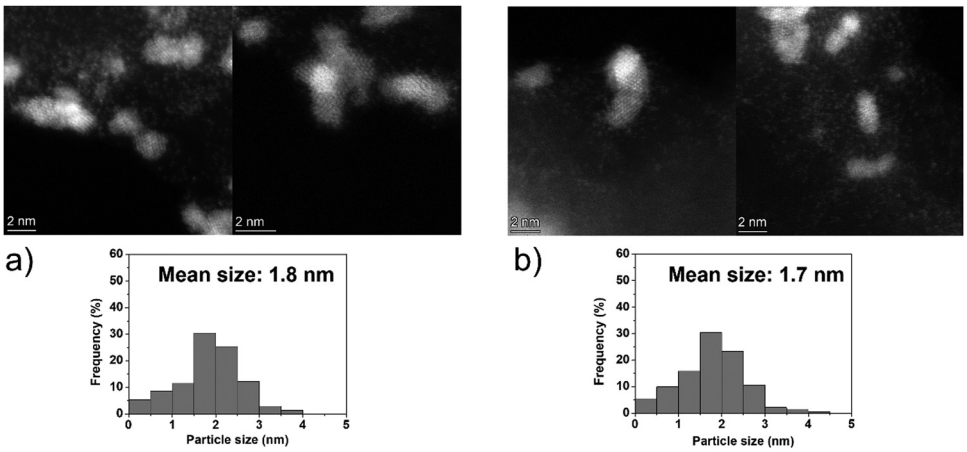

Fig. 5 Representative HAADF-STEM images and Ir particle size distribution of 1 wt% Ir/GCN, (a) fresh and (b) after 5 runs. Inset histograms show the particle size distribution.

Table 1 Results of survey spectra of fresh and used Ir catalysts

Samples	C1s/atomic%	N1s/atomic%	Ir4f/atomic%
Ir/graphite fresh	99.2	0.0	0.8
Ir/graphite 5 runs	98.5	1.2	0.3
Ir/GCN fresh	64.0	34.7	1.3
Ir/GCN 5 runs	65.2	33.8	1.0

Table 2 Results of HR C 1s and N 1s spectra analysis for the nitride samples indicating a decrease in the intensity ratio between C–N=C (285.5 eV) and C=C (288.8) and the increase between qN and C=N–H ratios with C=N after the immobilization of sub-nanometric Ir particles and used catalyst

Samples	$\left(\frac{I_{C-N-C}}{I_{C-C}}\right)$	$\left(\frac{I_{qN}}{I_{C=N}}\right)$	$\left(\frac{I_{C=N-H}}{I_{C=N}}\right)$
GCN	3.44	0.17	0.21
Ir/GCN fresh	1.67	0.20	0.29
Ir/GCN 1 run	1.44	0.19	0.28
Ir/GCN 5 run	1.43	0.19	0.29

Fig. 6 shows the Ir 4f regions of Ir/graphite and Ir/GCN. Three main contributions were included in the fitting: metallic (Ir^0), rutile-type (Ir^{IV}) and an Ir(IV)–OH component found in amorphous Ir oxyhydroxides, whose oxidation state is still unclear.[96,97] This species was found forming on a carbon support by electrodeposition from an $IrCl_3$ solution.[71] We consider this a Ir(IV)–OH specie at the surface of the nanoparticle, for simplicity referred to in the text as $Ir^{IV\text{-}OH}$. Ir^0, Ir^{IV} and $Ir^{IV\text{-}OH}$ $4f_{7/2}$ components were assigned respectively to BE of 60.75, 61.70 and 62.30 eV. In addition, Ir^{IV} and $Ir^{IV\text{-}OH}$ presented an asymmetric line shape and appeared in combination with satellite peaks at 1 eV higher BEs.

The Ir/graphite presented a lower $Ir^{IV\text{-}OH/IV}/Ir^0$ ratio than the Ir/GCN sample, indicating a higher number of metallic Ir fraction with respect to the nitride sample, which can be related to slightly larger particles. Previous studies attributed the higher ratio between the oxidized and metallic fractions to an enhanced reactivity of the particles leading to surface oxidation in air ($Ir^{IV\text{-}OH}/Ir^{IV}$) and to a stronger electronic interaction of the precursor with the support, making it more difficult to reduce to the metallic state.[98]

A detailed comparison of the HR Ir 4f of fresh Ir/graphite and Ir/GCN highlighted a negative shift in the Ir^0 peak (core level shift, CLS = −0.10 eV, Fig. 7) when GCN is employed as the

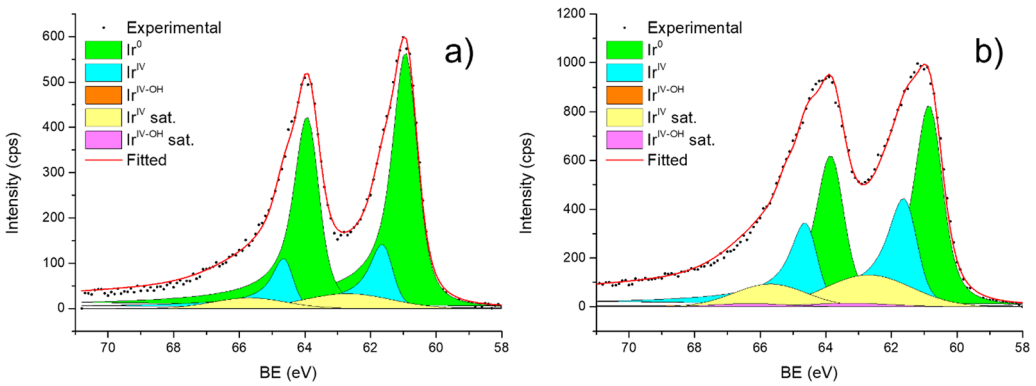

Fig. 6 Fitting of high-resolution spectra of Ir 4f in (a) Ir/graphite and (b) Ir/GCN fresh catalysts.

support. This shift indicates an increased electron density at the Ir sub-nanometric particles surface due to the N moieties of the support,[32,99] strengthening the Ir–support interaction. Indeed, the CLS agrees with the observed intensity ratio decrease between C–N═C and C═C peaks (Table 2 and Fig. S3, ESI†) and the comparison of $Ir^{IV\text{-}OH/IV}/Ir^{0}$ ratio (Fig. 1), highlighting an Ir–N interaction.

The analysis of the HR Ir 4f spectra for fresh and used samples included the Na 2s contribution, which overlaps with the Ir 4f of the used sample (Fig. S5, ESI†). The presence of adsorbed Na species on used samples is attributed to the solvent employed in the reaction, 0.5 M NaOH, which after 5 reaction runs significantly increased as shown by the magenta peak in Fig. S5 (ESI†). Nonetheless, a comparison of fresh and used samples for both the catalysts demonstrated a negative core level shift (CLS) of −0.10 eV in the $Ir^{0}_{7/2}$ BE of Ir/graphite after stability tests (Fig. 8), whereas no shift was observed for the other contributions ($Ir^{IV\text{-}OH}$, Ir^{IV}). These results support the deactivation of Ir/graphite due to residual adsorbates of the hydrous hydrazine decomposition reaction on the Ir active sites. In particular, it has been previously demonstrated that residual adsorbates lead to deactivation of the Ir catalyst.[100,101] Differently, no CLS was detected for the GCN supported catalysts (Fig. 8), suggesting improved resistance toward residual adsorbates of the hydrous hydrazine decomposition reaction.

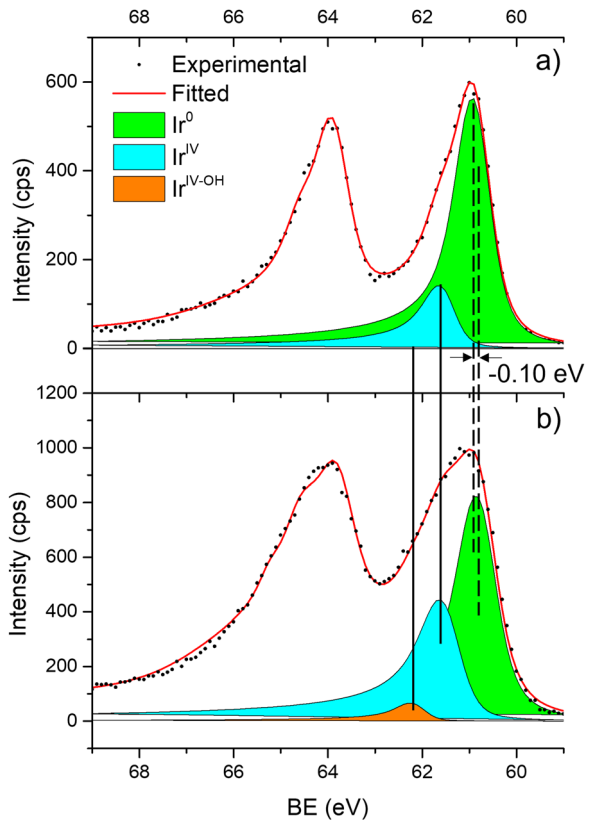

Fig. 7 High resolution Ir 4f spectra of fresh samples, (a) Ir/graphite and (b) Ir/GCN. For clarity, the comparison of the fitted contributions is limited to the $Ir_{7/2}$ components without any satellite.

In support of our assumption on catalyst poisoning, previous literature[69,102] demonstrated that residual NH_x (x = 1–2) and N_2H_x species can be detected in HR-XPS of the N 1s signal; in detail the N_2H_x nitrogen atom strongly bound to the metal surface and the one far away can be observed at BE of 400.2 and 401.5 eV respectively, while the NH_x (x = 1–2) signal is observable at BE of 398.6 eV. Thus, employing these models in an analysis of the N 1s region of the Ir/graphite samples, fresh and 5 runs used, was performed to confirm the preliminary results on catalyst poisoning, highlighting in the 5 runs used catalysts all the above-mentioned signals. Fig. 9 summarizes these results.

As expected, the fresh catalysts did not present any signal in the N 1s region, but on the other hand after 5 runs all the above-mentioned components are observed, namely, N_2H_x and NH_x. As stated by the authors the presence of N_2H_x and NH_x moieties respectively suggests a complete and an incomplete decomposition of $N_2H_4\cdots H_2O$.[69,102] Noticeably, the relative percentage area of the fitted contribution is in good agreement with the experimental selectivity observed for Ir/graphite used for 5 runs, where the catalysts resulted in 89% H_2 selectivity and presented a relative percentage area of complete decomposition adsorbed intermediates (N_2H_x) of 87%. Furthermore, this result agrees with the survey (Table 1) and the Ir 4f region (Fig. 8) analyses.

Thus, the higher initial catalytic activity of fresh Ir/graphite compared to Ir/GCN is attributed to a synergistic effect between the lower $Ir^{IV\text{-}OH/IV}/Ir^{0}$ (Fig. 1) and the localization of numerous NPs on the graphitic planes boundaries (Fig. S2, ESI†), recently reported to increase the NPs' reactivity with respect to the ones located on graphitic basal planes.103 For Ir/graphite, TEM images of the used sample showed slight coalescence (2.1 ± 0.5 nm, Fig. 4 and Fig. S3, ESI†). The XPS analysis suggested a deactivation of the catalyst due to residual adsorbates of the decomposition reaction, explained through survey data, supported by the detailed analysis of the $Ir^{0}_{7/2}$ peak performed, where a core level shift of −0.10 eV was observed compared to the fresh catalyst, and confirmed by the N 1s region analysis of the used samples, where an increasing content of residual decomposition adsorbates, namely NH_x and N_2H_x species was observed, but also to Ir leaching during the reaction.

Differently, Ir/GCN exhibited a lower decrease in Ir exposed (from 1.3% to 1.0) due to the partial adsorption of the reaction products on the active sites and better stabilized particles, and furthermore no Ir leaching was observed from the ICP-AES analysis. Overall, there are two beneficial effects of the presence of N anchoring sites: stabilizing the nanoparticles, therefore avoiding leaching, and preventing the active sites from deactivation under reaction conditions.

DFT results

Atomistic simulations were conducted to rationalise the superior performance, *i.e.*, resistance to poisoning and structural integrity, exhibited by the Ir particles supported on GCN compared to the graphite supported ones. PG and SV structures were chosen to model respectively an ideal basal plane and a

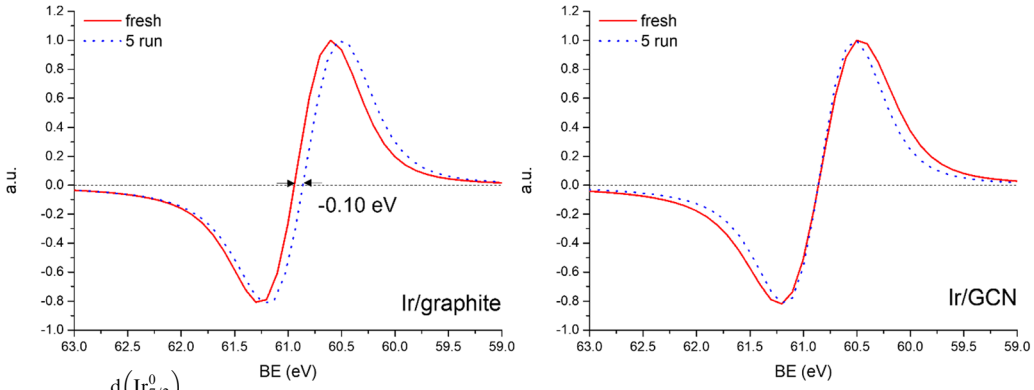

Fig. 8 Normalized derivative $\frac{d\left(Ir^{0}_{7/2}\right)}{dBE}$ of the Ir 4f spectra for Ir/graphite (left) and Ir/GCN (right).

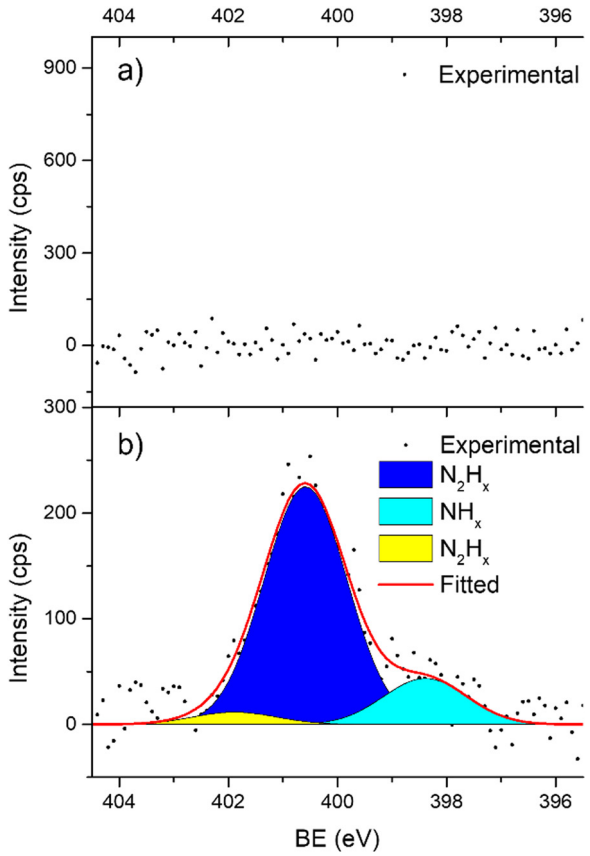

Fig. 9 High resolution N 1s spectra of Ir/graphite: (a) fresh and (b) used for 5 runs.

structure with undercoordinated C, typical from boundaries and intrinsic defects. This choice is supported by previous reports where SV was identified as the most reactive intrinsic punctual defect for adsorption processes.[65,104,105] With regard to GCN, the employed models (gN and 3pN) mimic its typical grafting sites, while maintaining a simplified representation of a realistic structure.[106,107] Modelling isolated functionalities, namely SV, gN and 3pN, in the carbon lattice is beneficial for the properties rationalization, especially in combination with experiments. Indeed, simplified models allowed an accurate investigation of the supported Ir nanoclusters resulting in a reliable and accurate analysis of the most stable geometries and related electronic structure.

Nanocluster adsorption

The geometries of modelled nanoclusters on the different surfaces were generated with the three-step Genetic Algorithm (GA) method described. Once the fittest candidates were obtained from the GA screening, different properties were computed and analysed to rationalize the experimental observations, *i.e.*, enhanced stability under reaction conditions and poisoning resistance.

Regarding the structural stability of the supported clusters, the presence of metal–support interactions influences the average bond length of the supported clusters, *e.g.*, Ir–Ir bond length, which is related to the strain against sintering processes. Recently, it has been proved that stronger adsorption of clusters correlates with the average metal–metal bond lengths in the cluster.[108,109] Thus, among the several descriptors available to analyse the structural stability of supported metal clusters, here, we have employed adsorption (E_{ads}, eqn (7)), adhesion (E_{adh}, eqn (8)) and surface deformation (E_{def}, eqn (9)) energies, together with the average Ir–Ir bond distance ($\overline{Ir-Ir}$), the support–cluster distance (d(C–S)), and the number of interfacial metal species (Ir_{IF}). Table 3 summarizes these results.

To obtain more precise information on the cluster support charge transfer, a detailed analysis of the charges flow after adsorption was performed together with a more qualitative representation, shown in Fig. 10. The evaluation of the Bader charges after adsorption (q_{clus}), the summation, q^{+}_{clus} and q^{-}_{clus}, and number of positive and negative charges, n_{q^+} and n_{q^-} localised in each Ir atom were evaluated. Table 4 summarizes the charge analysis.

To describe trends on the hydrazine decomposition process, Tafreshi and co-workers[110] unveiled a relationship between Cu surface site coordination number (CN) and hydrazine binding strength. Despite the effectiveness of this approach, when dealing with sub-nanometric clusters, a CN based analysis does not lead to reliable results due to intrinsic limitations of a simplistic model. Differently, the generalized coordination number (GCN) represents a more structure sensitive model capturing the weight averaged coordination of the adsorption

Table 3 Energetic and structural information for the interaction of Ir_{15} clusters with the supports. Adsorption energy (E_{ads}), adhesion energy (E_{adh}), deformation energy (E_{def}), cluster–support distance (d(C–S)), number of interfacial Ir species (Ir_{IF}), average generalized coordination number ($\overline{GCN}$) and average Ir–Ir bond distance ($\overline{Ir-Ir}$)

Support	Surface	E_{ads}/eV	E_{adh}/eV	E_{def}/eV	d(C–S)/Å	Ir_{IF}/n°	$\overline{Ir-Ir}$/Å	$\overline{GCN}$
Graphite	Ir_{15}/PG	−2.319	−1.731	−0.408	2.171	2	2.455	3.9
	Ir_{15}/SV	−10.641	−6.104	−4.536	1.077	2	2.425	3.7
GCN	Ir_{15}/gN	−3.968	−2.936	−1.032	1.910	3	2.521	4.6
	Ir_{15}/3pN	−5.716	−5.016	−0.701	1.168	2	2.432	3.7

site in facets, edges, vertices and other low-coordinated sites.[111] The GCN has been validated previously as an efficient catalytic activity descriptor due to its correlation with well-established descriptors such as the d-band center.[112,113] Thus, we decided to employ the average generalized coordination number ($\overline{GCN}$) as a descriptor for the catalytic activity toward hydrazine adsorption.

Structural stability

The Ir deposited on PG (graphitic basal plane) and on SV (under-coordinated carbons) models demonstrated an exothermic and favourable adsorption of the cluster (negative adsorption and adhesion energies). Nonetheless, the presence of low-coordinated sites on the SV models favours the Ir cluster adsorption with respect to the basal planes by $\Delta E_{ads}^{SV-PG} = -8.502$ and $\Delta E_{adh}^{SV-PG} = -4.374$ eV, which directly correlates to the surface deformation energies, $\Delta E_{def}^{SV-PG} = -4.128$ eV. This agrees with the TEM images where Ir NPs were preferentially located at the low-coordinated graphitic boundaries (Fig. S3, ESI†). Measured features like $\overline{Ir-Ir}$ and charge transfer also indicate a stronger interaction with undercoordinated carbon atoms due to the shorter cluster support distance and higher charge transfer to the support in the SV

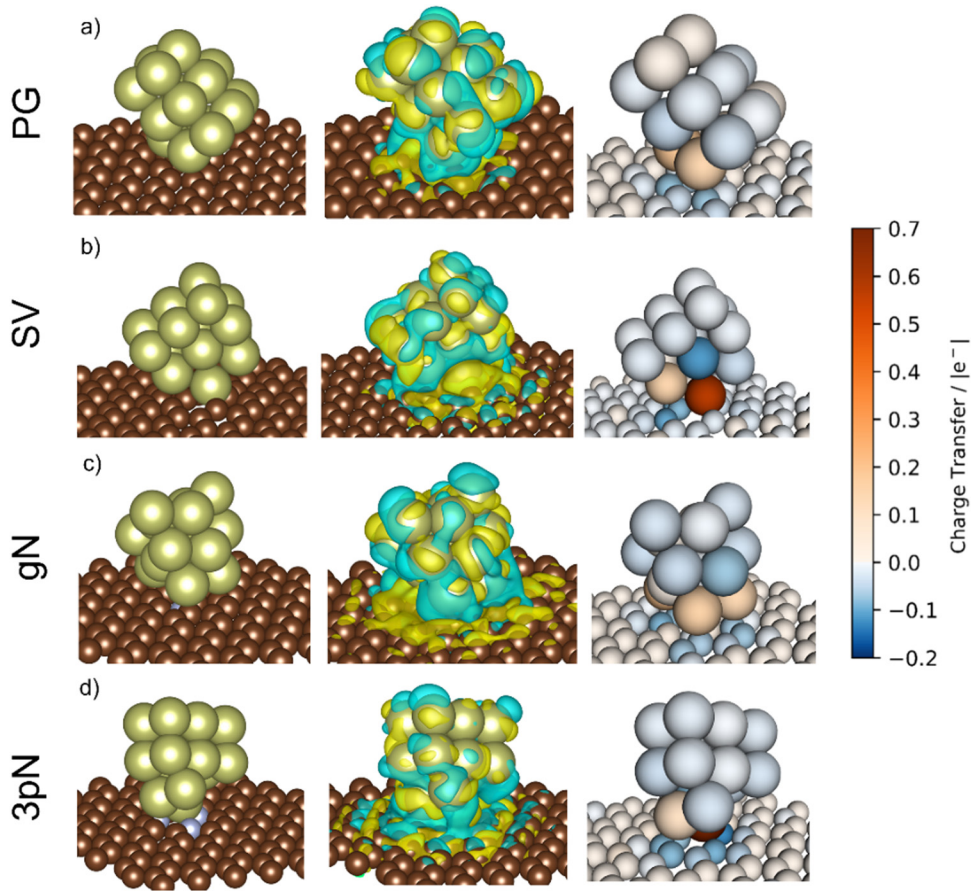

Fig. 10 Isometric view of the Ir_{15} cluster on (a) pristine graphene (PG), (b) single vacancy (SV), (c) graphitic-N (gN) and (d) triple pyridinic-N (3pN). From left to right panels: structure representation, charge density difference plot (CDDP), and Bader charge difference plot (BCDP). Left and center panels: carbon atoms are colored in brown, nitrogen in blue and iridium in yellow. Center panel: yellow and blue iso-surfaces denote gain and depletion of electron density respectively, and the iso-surface value is 3×10^{-4} e^{-} $Å^{-2}$. Right panel: Atom colors refer to the charge adsorption charge transfer extent, based on the proposed charge transfer colormap, and the positive and negative values denote depletion and gain of electrons, respectively.

Table 4 Bader charge analysis for the Ir_{15} clusters on each support. Total cluster charge redistributions (q_{clus}), total redistributed positive charges (q^{+}_{clus}), number of Ir atoms which gained positive charge (n_{q^+}), total redistributed negative charges (q^{-}_{clus}), and number of Ir atoms which gained negative charge (n_{q^-})

Support	Surface	$q_{clus}/\|e\|$	$q^{+}_{clus}/\|e\|$	n_{q^+}/n°	$q^{-}_{clus}/\|e\|$	n_{q^-}/n°
Graphite	Ir_{15}/PG	0.22	0.41	5	−0.19	8
	Ir_{15}/SV	0.47	0.73	3	−0.25	12
GCN	Ir_{15}/gN	0.22	0.51	6	−0.29	9
	Ir_{15}/3pN	0.47	0.79	2	−0.31	13

than in the PG model. Indeed, although the Ir cluster morphology on the graphite models (PG and SV) is similar and both interact with the support with two Ir atoms, the charge transfer on SV is enhanced by the interaction of the cluster and the carbon dangling bonds compared to PG (Fig. 10). This enhanced charge transfer of the SV model directly correlates with the difference observed in the stability descriptors employed (E_{ads}, E_{adh}, E_{def}, d(C–S), Table 4). The analysis performed allowed us to individuate low-coordinated carbons as mainly responsible for the cluster stabilization, *i.e.*, coalescence prevention, due to an enhanced cluster to support charge transfer which resulted in improved adsorption, adhesion, and surface deformation energies, as well as closer cluster–support distance.

We can conclude that clusters immobilized on the PG model easily migrate to the SV sites, which in opposition are strongly anchored to the support. This is in good agreement with the TEM analysis performed on the Ir/graphite catalyst, where particles located at graphite plane boundaries were observed, exhibiting slight coalescence after 5 reaction runs.

The two N containing models (gN and 3pN) presented exothermic and favourable adsorption of the Ir clusters. The adsorption on the 3pN model resulted in more exothermic adsorption, $\Delta E_{ads}^{3pN-gN} = -1.748$ eV, and adhesion, $\Delta E_{adh}^{3pN-gN} = -2.080$ eV, energies than the gN model. These results highlight an enhanced stabilization of clusters deposited on the heptazine rings (3pN) with respect to the graphitic N (gN), in agreement with the cluster–support distance analysed. The Ir cluster is closer to 3pN than to gN, despite the former presenting less interfacial Ir species ($Ir_{IF} = 2$) than the latter ($Ir_{IF} = 3$) due to, on gN, Ir interacting with C atoms vicinal to the graphitic N.[114] Nonetheless, the Ir cluster on 3pN presents an enhanced cluster–support charge transfer compared to the gN one, although both models present a higher extent of negative charge distributed on the support compared to the graphite ones, well indicating an increased cluster–support interaction. This can be clearly seen on the charge density difference (CDD) analysis in Fig. 10. The structural and energetic analysis of the cluster immobilized on the gN and 3pN models allowed us to individuate the N moieties of GCN as the main one responsible for the cluster stabilization due to an enhanced cluster–support interaction. Indeed, the GCN models resulted in better stabilization of the clusters on both the studied surfaces, gN and 3pN, compared to the less-stabilizing of the graphite models, PG, which has also been individuated as the main one responsible for the Ir/graphite coalescence.

Overall, although in both systems best cluster stabilization was obtained on low-coordination sites (SV for graphite and 3pN for GCN), it is now clear that graphitic N (gN) supported clusters are better prevented from coalescence toward the 3pN deposed ones. Therefore, considering the supported cluster stability descriptors analysed and the charge-transfer studies performed, it was possible to rationalize the differences observed in TEM particle size distributions for Ir/graphite and Ir/GCN after stability tests.

Catalytic activity and poisoning resistance

According to previous studies in the literature,[103] a low $\overline{GCN}$ and a contraction of cluster interatomic distances leads to an increased catalytic activity. This expected behaviour is confirmed when comparing Ir_{15} clusters on SV and PG (Table 3) and considering the experimental values for the first run of Ir/graphite (4071 h^{-1}).

On the GCN models the analysis of $\overline{GCN}$ and $\overline{Ir-Ir}$ values (Table 3) suggest an enhanced reactivity of Ir clusters on 3pN compared to gN, which fully agrees with the catalytic activity of Ir/GCN (3675 h^{-1}) when considering that the most stable clusters are the ones on the 3pN model. Thus, the simulation of graphite and GCN models were able to describe the experimental initial catalytic activity by employing $\overline{GCN}$ and $\overline{Ir-Ir}$ as reactivity descriptors, in agreement with recent computational studies on Pt clusters supported on carbonaceous materials.[115] Furthermore, the comparison between Ir/graphite and Ir/GCN models in terms of $\overline{GCN}$ and $\overline{Ir-Ir}$ agrees with the higher catalytic activity observed (4024 h^{-1} and 3654 h^{-1}, respectively) for the sub-nanometric Ir supported on graphite.

Previous studies on the hydrous hydrazine decomposition performed over supported Ir catalysts demonstrated that the metal clusters' catalytic activity may decline due to the adsorption of residual decomposition intermediates, leading to poisoning of the active sites and catalyst deactivation. The authors were able to demonstrate that this can be substantially reduced when H_2 is admixed to the reaction environment, namely, in the presence of a stronger reducing atmosphere favouring further decomposition of the residual adsorbates.[100,102] Due to the experimental setup employed in this work, it was not possible to verify this hypothesis from the experiments. Nonetheless, quantitative analysis of the Bader charges performed (Table 4) provided detailed electronic information explaining the different catalytic performances of Ir/graphite and Ir/GCN.

The clusters on PG and SV models (graphite) both transferred electrons to the support after deposition, respectively 0.22 and 0.47 $|e^-|$ (Table 4). In the case of SV, the high electron transfer derives from the presence of carbon dangling bonds, *i.e.*, unpaired electrons,[109] which lead to more atoms with negative charges ($n_{q^-} = 12$, $q^{-}_{clus} = -0.25\ |e^-|$) distributed within the cluster (Fig. 10) compared to PG ($n_{q^-} = 8$, $q^{-}_{clus} = -0.19\ |e^-|$).

Thanks to a stronger cluster–support interaction of the SV model, the redistribution of negative charges on the cluster's surface, *i.e.*, more reducing interfaces, can better disfavour the formation of the undesired bound intermediates compared to

the PG model, which is more prone to undergoing poisoning of the active sites due to a weaker cluster–support interaction that resulted in less redistributed negative charges, as can be clearly seen in Fig. 10.

The presence of N on the GCN models led to a redistribution of the charges differently to the graphite models even though a similar charge transferred. The cluster supported on the gN model presented several atoms with a positive charge at the cluster–support interface (n_{q^+} = 6, q^+_{clus} = 0.51 $|e^-|$), which is clearly seen on the charge density difference (CDD) analysis in Fig. 10, and a high number of negative charges distributed on the cluster surface (n_{q^-} = 9, q^-_{clus} = −0.29 $|e^-|$). In the 3pN model the support to cluster charge transfer is enhanced with respect to gN (Table 4). This charge transfer is due to the pyridinic N sites, leading to strongly localized positive charges at the cluster–support interface (n_{q^+} = 2, q^+_{clus} = 0.79 $|e^-|$), in agreement with recent computational studies,[116,117] along with the highest number of negative charges distributed on the cluster surface (n_{q^-} = 13, q^-_{clus} = −0.31 $|e^-|$), as shown in Fig. 10. Noticeably, both the GCN models exhibited a higher value of redistributed negative charges (q^-_{clus} = −0.29 and −0.31 $|e^-|$, respectively for gN and 3pN) compared to the graphite models (q^-_{clus} = −0.19 and −0.25 $|e^-|$, respectively for PG and SV). The presence of N moieties (gN and 3pN) leads to a stronger redistribution of charges within the clusters, with a higher extent of negative charges, *i.e.*, electrons, on the cluster surfaces for both the gN and the 3pN models compared to the graphite models (PG and SV). These results agree with the XPS core level shift of −0.10 eV observed for the fresh catalysts and help to understand the enhanced poisoning resistance exhibited by Ir/GCN upon repeated reaction runs. Overall, the more electron-rich the clusters, the better is their resistance to poisoning by decomposition intermediates, *e.g.*, N_2H_x and NH_x.

Conclusions

A combination of computational and experimental studies was employed to disclose the role of GCN functionalities in enhancing the stability of sub-nanometric iridium particles during the hydrous hydrazine decomposition reaction. Two different catalysts were synthesized using a modified wet impregnation method, 1 wt% Ir/graphite and 1 wt% Ir/GCN. Both the fresh catalysts exhibited remarkable initial catalytic activities (3654 h^{-1} and 4024 h^{-1} for Ir/GCN and Ir/graphite, respectively) and H_2 selectivity (94 and 95%). The hydrous hydrazine decomposition kinetic profiles evidenced an enhanced stability of the Ir/GCN samples upon repeated reaction cycles with respect to Ir/graphite. TEM and XPS analyses showed that the deactivation of Ir/graphite can be attributed to partial irreversible adsorption of the reaction products (XPS core level shift in Ir^0 of −0.10 eV after 5 runs and residual adsorbates detected in the N 1s region), Ir leaching and a partial aggregation of Ir particles, for those with a size <2 nm. On the other hand, Ir/GCN exhibited a higher stability, without significant modification of the structure of the catalyst. This result was rationalized at an atomic scale level through a combined TEM, XPS and DFT analysis and attributed to an enhanced metal–support interaction related to the N grafting sites of GCN. Low-coordinated carbons (SV) can efficiently adsorb and stabilize Ir clusters, better than the basal planes (PG) which drives the cluster agglomeration under reaction conditions. On the other hand, both the basal plane N (gN) and the heptazine rings (3pN) in GCN have a strong interaction with the clusters, minimising the thermodynamic driving force for their coalescence. In addition, a detailed analysis of the Bader charges of the supported Ir clusters revealed that the presence of N moieties on the support promotes a charge redistribution that enhances structural integrity and explains the poisoning resistance in terms of the electron enriched cluster surface. In conclusion, the combined experimental–computational approach allowed us to assign the GCN nitrogen anchoring sites as the main ones responsible for the sub-nanometric particle integrity and improved stability, and to rationalize the experimental reactivity and characterization results in terms of metal–support interactions.

Conflicts of interest

There are no conflicts to declare.

Acknowledgements

We acknowledge computing time on the facilities of Supercomputing Wales and the Advanced Research Computing Cardiff (ARCCA) at Cardiff University. This work is partially supported by the project with the reference number PID2020-113809RB-C33 from the Ministry of Science, Innovation and Universities of Spain. S. B. thanks Dr S. Cattaneo for the fruitful discussions. This work is partially supported by the project with reference RV_PSR_SOE_2020_AVILL, Piano Sviluppo Unimi – Linea 3 – Bando SoE.

References

1 M. Besson, P. Gallezot and C. Pinel, *Chem. Rev.*, 2014, **114**, 1827–1870.
2 E. Gianotti, M. Taillades-Jacquin, J. Rozière and D. J. Jones, *ACS Catal.*, 2018, **8**, 4660–4680.
3 M. Che and C. O. Bennett, *Advances in Catalysis*, Elsevier, 1989, vol. 36, pp. 55–172.
4 T. S. Rodrigues, A. G. M. da Silva and P. H. C. Camargo, *J. Mater. Chem. A*, 2019, **7**, 5857–5874.
5 I. MacLaren and Q. M. Ramasse, *Int. Mater. Rev.*, 2014, **59**, 115–131.
6 S. J. Pennycook, M. F. Chisholm, A. R. Lupini, M. Varela, A. Y. Borisevich, M. P. Oxley, W. D. Luo, K. van Benthem, S.-H. Oh and D. L. Sales, *Philos. Trans. R. Soc., A*, 2009, **367**, 3709–3733.
7 B. Zandkarimi and A. N. Alexandrova, *Wiley Interdiscip. Rev.: Comput. Mol. Sci.*, 2019, **9**, 1–17.
8 Z. Zhang, B. Zandkarimi and A. N. Alexandrova, *Acc. Chem. Res.*, 2020, **53**, 447–458.

9 L. Liu and A. Corma, *Chem. Rev.*, 2018, **118**, 4981–5079.
10 J. D. Aiken and R. G. Finke, *Chem. Mater.*, 1999, **11**, 1035–1047.
11 A. L. Maksimov, S. N. Kuklin, Y. S. Kardasheva and E. A. Karakhanov, *Pet. Chem.*, 2013, **53**, 157–163.
12 S. M. Rogers, C. R. A. Catlow, C. E. Chan-Thaw, A. Chutia, N. Jian, R. E. Palmer, M. Perdjon, A. Thetford, N. Dimitratos and A. Villa, *ACS Catal.*, 2017, **7**, 2266–2274.
13 C. T. Campbell, *Acc. Chem. Res.*, 2013, **46**, 1712–1719.
14 C. T. Campbell, S. C. Parker and D. E. Starr, *Science*, 2002, **298**, 811–814.
15 X. Wang, G. Sun, P. Routh, D.-H. Kim, W. Huang and P. Chen, *Chem. Soc. Rev.*, 2014, **43**, 7067–7098.
16 M. S. Shafeeyan, W. M. A. W. Daud, A. Houshmand and A. Arami-Niya, *Appl. Surf. Sci.*, 2011, **257**, 3936–3942.
17 M. S. Shafeeyan, W. M. A. W. Daud, A. Houshmand and A. Shamiri, *J. Anal. Appl. Pyrolysis*, 2010, **89**, 143–151.
18 C. Rivera-Cárcamo and P. Serp, *ChemCatChem*, 2018, **10**, 5058–5091.
19 S. Li, X. Lu, S. Zhao, M. Ceccato, X.-M. Hu, A. Roldan, M. Liu and K. Daasbjerg, *ACS Catal.*, 2022, **12**, 7386–7395.
20 Y. Hou, M. Qiu, M. G. Kim, P. Liu, G. Nam, T. Zhang, X. Zhuang, B. Yang, J. Cho and M. Chen, *Nat. Commun.*, 2019, **10**, 1–9.
21 X. Zhou, X. Liu, J. Zhang, C. Zhang, S. J. Yoo, J.-G. Kim, X. Chu, C. Song, P. Wang and Z. Zhao, *Carbon N. Y.*, 2020, **166**, 284–290.
22 X. Xing, R. Liu, M. Anjass, K. Cao, U. Kaiser, G. Zhang and C. Streb, *Appl. Catal., B*, 2020, **277**, 119195.
23 J. Hao, W. Yang, Z. Peng, C. Zhang, Z. Huang and W. Shi, *ACS Catal.*, 2017, **7**, 4214–4220.
24 H. Li, L. Chen, P. Jin, Y. Li, J. Pang, J. Hou, S. Peng, G. Wang and Y. Shi, *Nano Res.*, 2022, **15**, 950–958.
25 S. K. Singh, K. Takeyasu and J. Nakamura, *Adv. Mater.*, 2019, **31**, 1804297.
26 H. Liu, X. Wu, Y. Geng, X. Li and J. Xu, *Green Energy Environ.*, 2022, DOI: **10.1016/j.gee.2022.09.001**.
27 J. H. Kim, J. Y. Cheon, T. J. Shin, J. Y. Park and S. H. Joo, *Carbon N. Y.*, 2016, **101**, 449–457.
28 I. Barlocco, S. Bellomi, J. J. Delgado, X. Chen, L. Prati, N. Dimitratos, A. Roldan and A. Villa, *Catal. Today*, 2021, **382**, 61–70.
29 Q. Wang, N. Tsumori, M. Kitta and Q. Xu, *ACS Catal.*, 2018, **8**, 12041–12045.
30 D. Liu, X. Chen, G. Xu, J. Guan, Q. Cao, B. Dong, Y. Qi, C. Li and X. Mu, *Sci. Rep.*, 2016, **6**, 1–13.
31 X. Wu, B. Feng, W. Li, Y. Niu, Y. Yu, S. Lu, C. Zhong, P. Liu, Z. Tian and L. Chen, *Nano Energy*, 2019, **62**, 117–126.
32 L. Yi, B. Feng, N. Chen, W. Li, J. Li, C. Fang, Y. Yao and W. Hu, *Chem. Eng. J.*, 2021, **415**, 129034.
33 D. Liu, X. Chen, G. Xu, J. Guan, Q. Cao, B. Dong, Y. Qi, C. Li, X. Mu, X. Wu, B. Feng, W. Li, Y. Niu, Y. Yu, S. Lu, C. Zhong, P. Liu, Z. Tian, L. Chen, A. Iemhoff, M. Vennewald, J. Artz, C. Mebrahtu, A. Meledin, T. E. Weirich, H. Hartmann, A. Besmehn, M. Aramini, F. Venturini, Z. Li, Y. Chen, S. Ji, Y. Tang, W. Chen, A. Li, J. Zhao, Y. Y. Xiong, Y. Wu, Y. Gong, J. Shen, H. Wu, W. Sun, J. Qiao, H. Cai, Z. Wang, K. Sun, L. Yi, B. Feng, N. Chen, W. Li, J. Li, C. Fang, Y. Yao, W. Hu, X. Xiao, H. Zhang, Y. Y. Xiong, F. Liang and Y. Yang, *Chem. Eng. J.*, 2021, **6**, 764–772.
34 J. Shen, H. Wu, W. Sun, J. Qiao, H. Cai, Z. Wang and K. Sun, *Chem. Eng. J.*, 2019, **358**, 340–350.
35 Q. Tian, Z. Zhou, R. Wang, J. Zhang and C. Wang, *J. Alloys Compd.*, 2022, **918**, 165523.
36 X. Shao, X. Yang, J. Xu, S. Liu, S. Miao, X. Liu, X. Su, H. Duan, Y. Huang and T. Zhang, *Chem*, 2019, **5**, 693–705.
37 D. Nandi, S. Siwal, M. Choudhary and K. Mallick, *Appl. Catal., A*, 2016, **523**, 31–38.
38 W. Xue, W. Chang, X. Hu, J. Fan, X. Bai and E. Liu, *J. Colloid Interface Sci.*, 2020, **576**, 203–216.
39 H. Starukh, M. Koštejn, V. Matějka and P. Praus, *Nanoscale Res. Lett.*, 2021, **16**, 1–14.
40 A. Iemhoff, M. Vennewald, J. Artz, C. Mebrahtu, A. Meledin, T. E. Weirich, H. Hartmann, A. Besmehn, M. Aramini, F. Venturini, F. W. Mosselmans, G. Held, R. Arrigo and R. Palkovits, *ChemCatChem*, 2022, **14**(9), DOI: **10.1002/cctc.202200179**.
41 Z. Chen, S. Mitchell, E. Vorobyeva, R. K. Leary, R. Hauert, T. Furnival, Q. M. Ramasse, J. M. Thomas, P. A. Midgley and D. Dontsova, *Adv. Funct. Mater.*, 2017, **27**, 1605785.
42 X. Li, P. Cui, W. Zhong, J. Li, X. Wang, Z. Wang and J. Jiang, *Chem. Commun.*, 2016, **52**, 13233–13236.
43 X. Jiang, L. Zhang, H. Liu, D. Wu, F. Wu, L. Tian, L. Liu, J. Zou, S. Luo and B. Chen, *Angew. Chem., Int. Ed.*, 2020, **132**, 23312–23316.
44 Q. Bing and J. Liu, *Appl. Surf. Sci.*, 2021, **562**, 150186.
45 N. N. Zhang, J. Li and H. Xiao, *ChemCatChem*, 2022, **14**(16), DOI: **10.1002/cctc.202200275**.
46 Z. Zhao, Y. Sun and F. Dong, *Nanoscale*, 2015, **7**, 15–37.
47 T. Yuan, H. Gong, K. Kailasam, Y. Zhao, A. Thomas and J. Zhu, *J. Catal.*, 2015, **326**, 38–42.
48 S. K. Singh and Q. Xu, *J. Am. Chem. Soc.*, 2009, **131**, 18032–18033.
49 S. K. Singh, Z. H. Lu and Q. Xu, *Eur. J. Inorg. Chem.*, 2011, 2232–2237.
50 J. K. Norskov and C. H. Christensen, *Science*, 2006, **312**, 1322–1323.
51 Z. Zhang, S. Zhang, Q. Yao, X. Chen and Z.-H. Lu, *Inorg. Chem.*, 2017, **56**, 11938–11945.
52 S. J. Cho, J. Lee, Y. S. Lee and D. P. Kim, *Catal. Lett.*, 2006, **109**, 181–186.
53 A. K. Singh, M. Yadav, K. Aranishi and Q. Xu, *Int. J. Hydrogen Energy*, 2012, **37**, 18915–18919.
54 P.-X. Zhang, Y.-G. Wang, Y.-Q. Huang, T. Zhang, G.-S. Wu and J. Li, *Catal. Today*, 2011, **165**, 80–88.
55 L. Zhou, X. Luo, L. Xu, C. Wan and M. Ye, *Catalysts*, 2020, **10**(8), DOI: **10.3390/catal10080930**.
56 L. He, B. Liang, L. Li, X. Yang, Y. Huang, A. Wang, X. Wang and T. Zhang, *ACS Catal.*, 2015, **5**, 1623–1628.
57 D. Motta, I. Barlocco, S. Bellomi, A. Villa and N. Dimitratos, *Nanomaterials*, 2021, **11**, 1340.
58 K. S. Sanjay, X. B. Zhang and Q. Xu, *J. Am. Chem. Soc.*, 2009, **131**, 9894–9895.

59 X. Lu, S. Francis, D. Motta, N. Dimitratos and A. Roldan, *Phys. Chem. Chem. Phys.*, 2020, **22**, 3883–3896.
60 Y. B. Jang, T. H. Kim, M. H. Sun, J. Lee and S. J. Cho, *Catal. Today*, 2009, **146**, 196–201.
61 F. Goettmann, A. Fischer, M. Antonietti and A. Thomas, *Chem. Commun.*, 2006, 4530–4532.
62 M. Roselló-Merino, R. J. Rama, J. Díez and S. Conejero, *Chem. Commun.*, 2016, **52**, 8389–8392.
63 L. Luconi, E. S. Osipova, G. Giambastiani, M. Peruzzini, A. Rossin, N. V. Belkova, O. A. Filippov, E. M. Titova, A. A. Pavlov and E. S. Shubina, *Organometallics*, 2018, **37**, 3142–3153.
64 A. Telleria, P. W. N. M. van Leeuwen and Z. Freixa, *Dalton Trans.*, 2017, **46**, 3569–3578.
65 I. Barlocco, S. Bellomi, S. Tumiati, P. Fumagalli, N. Dimitratos, A. Roldan and A. Villa, *Phys. Chem. Chem. Phys.*, 2022, **24**, 3017–3029.
66 C. R. Harris, K. J. Millman, S. J. Van Der Walt, R. Gommers, P. Virtanen, D. Cournapeau, E. Wieser, J. Taylor, S. Berg and N. J. Smith, *Nature*, 2020, **585**, 357–362.
67 P. Virtanen, R. Gommers, T. E. Oliphant, M. Haberland, T. Reddy, D. Cournapeau, E. Burovski, P. Peterson, W. Weckesser and J. Bright, *Nat. Methods*, 2020, **17**, 261–272.
68 A. I. Large, S. Wahl, S. Abate, I. da Silva, J. J. Delgado Jaen, N. Pinna, G. Held and R. Arrigo, *Catalysts*, 2020, 10.
69 D. J. Alberas, J. Kiss, Z. M. Liu and J. M. White, *Surf. Sci.*, 1992, **278**, 51–61.
70 R. Arrigo, R. Blume, V. Streibel, C. Genovese, A. Roldan, M. E. Schuster, C. Ampelli, S. Perathoner, J. J. Velasco Vélez and M. Hävecker, *ACS Catal.*, 2021, **12**, 411–430.
71 V. Streibel, M. Hävecker, Y. Yi, J. J. Velasco Vélez, K. Skorupska, E. Stotz, A. Knop-Gericke, R. Schlögl and R. Arrigo, *Top. Catal.*, 2018, **61**, 2064–2084.
72 G. Kresse and J. Furthmüller, *Phys. Rev. B: Condens. Matter Mater. Phys.*, 1996, **54**, 11169–11186.
73 G. Kresse, *J. Non-Cryst. Solids*, 1995, **192–193**, 222–229.
74 I. Fampiou and A. Ramasubramaniam, *J. Phys. Chem. C*, 2015, **119**, 8703–8710.
75 R. Sure, J. Antony and S. Grimme, *J. Phys. Chem. B*, 2014, **118**, 3431–3440.
76 S. Ehrlich, J. Moellmann, W. Reckien, T. Bredow and S. Grimme, *ChemPhysChem*, 2011, **12**, 3414–3420.
77 H. Fang, A. Roldan, C. Tian, Y. Zheng, X. Duan, K. Chen, L. Ye, S. Leoni and Y. Yuan, *J. Catal.*, 2019, **369**, 283–295.
78 X. Lu, S. Francis, D. Motta, N. Dimitratos and A. Roldan, *Phys. Chem. Chem. Phys.*, 2020, **22**, 3883–3896.
79 E. Nowicka, S. Althahban, T. D. Leah, G. Shaw, D. Morgan, C. J. Kiely, A. Roldan and G. J. Hutchings, *Sci. Technol. Adv. Mater.*, 2019, **20**, 367–378.
80 M. G. Quesne, A. Roldan, N. H. De Leeuw and C. R. A. Catlow, *Phys. Chem. Chem. Phys.*, 2019, **21**, 10750–10760.
81 J. D. Pack and H. J. Monkhorst, *Phys. Rev. B: Solid State*, 1977, **16**, 1748–1749.
82 K. Momma and F. Izumi, *J. Appl. Crystallogr.*, 2011, **44**, 1272–1276.
83 J. D. Hunter, *Comput. Sci. Eng.*, 2007, **9**, 90–95.
84 P. Ramachandran and G. Varoquaux, *Comput. Sci. Eng.*, 2011, **13**, 40–51.
85 A. H. Larsen, J. J. Mortensen, J. Blomqvist, I. E. Castelli, R. Christensen, M. Dułak, J. Friis, M. N. Groves, B. Hammer and C. Hargus, *J. Phys.: Condens. Matter*, 2017, **29**, 273002.
86 P. Raybaud, C. Chizallet, C. Mager-Maury, M. Digne, H. Toulhoat and P. Sautet, *J. Catal.*, 2013, **308**, 328–340.
87 C.-C. Chang, C.-Y. Liu and Y.-C. Sun, *Phys. Chem. Chem. Phys.*, 2020, **22**, 4967–4973.
88 A. F. Yonezawa, G. R. Nagurniak, R. P. Orenha, E. H. da Silva, R. L. T. Parreira and M. J. Piotrowski, *J. Phys. Chem. A*, 2021, **125**, 4805–4818.
89 I. Barlocco, S. Capelli, X. Lu, S. Bellomi, X. Huang, D. Wang, L. Prati, N. Dimitratos, A. Roldan and A. Villa, *ChemCatChem*, 2021, **13**, 4210–4222.
90 J. Engel, S. Francis and A. Roldan, *Phys. Chem. Chem. Phys.*, 2019, **21**, 19011–19025.
91 J. B. A. Davis, A. Shayeghi, S. L. Horswell and R. L. Johnston, *Nanoscale*, 2015, **7**, 14032–14038.
92 A. Villa, S. J. Freakley, M. Schiavoni, J. K. Edwards, C. Hammond, G. M. Veith, W. Wang, D. Wang, L. Prati and N. Dimitratos, *Catal. Sci. Technol.*, 2016, **6**, 694–697.
93 B. Yue, Q. Li, H. Iwai, T. Kako and J. Ye, *Sci. Technol. Adv. Mater.*, 2011, **12**(3), DOI: **10.1088/1468-6996/12/3/034401**.
94 T. S. Miller, A. B. Jorge, T. M. Suter, A. Sella, F. Corà and P. F. McMillan, *Phys. Chem. Chem. Phys.*, 2017, **19**, 15613–15638.
95 J. Fu, B. Zhu, C. Jiang, B. Cheng, W. You and J. Yu, *Small*, 2017, **13**, 1603938.
96 V. Pfeifer, T. E. Jones, J. J. V. Vélez, R. Arrigo, S. Piccinin, M. Hävecker, A. Knop-Gericke and R. Schlögl, *Chem. Sci.*, 2017, **8**, 2143–2149.
97 V. Pfeifer, T. E. Jones, J. J. Velasco Vélez, C. Massué, R. Arrigo, D. Teschner, F. Girgsdies, M. Scherzer, M. T. Greiner and J. Allan, *Surf. Interface Anal.*, 2016, **48**, 261–273.
98 Z. Li, X. Yang, N. Tsumori, Z. Liu, Y. Himeda, T. Autrey and Q. Xu, *ACS Catal.*, 2017, **7**, 2720–2724.
99 H. Wang, M. Ming, M. Hu, C. Xu, Y. Wang, Y. Zhang, D. Gao, J. Bi, G. Fan and J.-S. Hu, *ACS Appl. Mater. Interfaces*, 2018, **10**, 22340–22347.
100 R. T. Rewick, B. J. Wood and H. Wise, *J. Phys. Chem.*, 1979, **83**, 2480–2485.
101 W. P. Krekelberg, J. Greeley and M. Mavrikakis, *J. Phys. Chem. B*, 2004, **108**, 987–994.
102 A. C. M. Van Den Broek, J. Van Grondelle and R. A. Van Santen, *J. Catal.*, 1999, **185**, 297–306.
103 H. Zhong, T. Wang, Y. Mo, C. Zheng and Y. Chen, *Electrochim. Acta*, 2022, **404**, 139602.
104 P. A. Denis and F. Iribarne, *J. Phys. Chem. C*, 2013, **117**, 19048–19055.
105 I. Barlocco, S. Capelli, X. Lu, S. Tumiati, N. Dimitratos, A. Roldan and A. Villa, *Nanoscale*, 2020, **12**, 22768–22777.
106 N. Rono, J. K. Kibet, B. S. Martincigh and V. O. Nyamori, *Crit. Rev. Solid State Mater. Sci.*, 2021, **46**, 189–217.

107 F. Fina, S. K. Callear, G. M. Carins and J. T. S. Irvine, *Chem. Mater.*, 2015, **27**, 2612–2618.
108 H. Shi, S. M. Auerbach and A. Ramasubramaniam, *J. Phys. Chem. C*, 2016, **120**, 11899–11909.
109 I. Fampiou and A. Ramasubramaniam, *J. Phys. Chem. C*, 2012, **116**, 6543–6555.
110 S. S. Tafreshi, A. Roldan and N. H. De Leeuw, *J. Phys. Chem. C*, 2014, **118**, 26103–26114.
111 A. S. Nair and B. Pathak, *Wiley Interdiscip. Rev.: Comput. Mol. Sci.*, 2021, **11**, e1508.
112 F. Calle-Vallejo, D. Loffreda, M. Koper and P. Sautet, *Nat. Chem.*, 2015, **7**, 403–410.
113 F. Calle-Vallejo, J. I. Martínez, J. M. García-Lastra, P. Sautet and D. Loffreda, *Angew. Chem., Int. Ed.*, 2014, **53**, 8316–8319.
114 S. Campisi, C. E. Chan-Thaw and A. Villa, *Appl. Sci.*, 2018, **8**, 1159.
115 Z. Jia, M. Peng, X. Cai, Y. Chen, X. Chen, F. Huang, L. Zhao, J. Diao, N. Wang and D. Xiao, *ACS Catal.*, 2022, **12**, 9602–9610.
116 Z. Li, Y. Chen, S. Ji, Y. Tang, W. Chen, A. Li, J. Zhao, Y. Xiong, Y. Wu and Y. Gong, *Nat. Chem.*, 2020, **12**, 764–772.
117 C. Jin, L. Cheng, G. Feng, R. Ye, Z.-H. Lu, R. Zhang and X. Yu, *Langmuir*, 2022, **38**, 3694–3710.